Title

Observation of hydrodynamic plasmons and energy waves in graphene

Journal

Nature, 614(7949)

ISSN

0028-0836

Authors

Zhao, Wenyu

Wang, Shaoxin

Chen, Sudi

et al.

Publication Date

2023-02-23

DOI

10.1038/s41586-022-05619-8

Observation of hydrodynamic plasmons and energy waves in graphene

Wenyu Zhao[1]†, Shaoxin Wang[1,2]†, Sudi Chen[3], Zuocheng Zhang[1], Kenji Watanabe[4], Takashi Taniguchi[5], Alex Zettl[1,3,6], Feng Wang[1,3,6*]

[1] Department of Physics, University of California at Berkeley, Berkeley, California 94720, United States.

[2] Graduate Group in Applied Science and Technology, University of California at Berkeley, Berkeley, California 94720, United States.

[3] Kavli Energy NanoScience Institute at University of California Berkeley and Lawrence Berkeley National Laboratory, Berkeley, California 94720, United States.

[4] Research Center for Functional Materials, National Institute for Materials Science, 1-1 Namiki, Tsukuba, 305-0044, Japan.

[5]International Center for Materials Nanoarchitectonics, National Institute for Materials Science, 1-1 Namiki, Tsukuba, 305-0044, Japan.

[6] Materials Sciences Division, Lawrence Berkeley National Laboratory, Berkeley, California, USA.

† These authors contributed equally to this work

* Correspondence to: fengwang76@berkeley.edu

Abstract:

Thermally excited electrons and holes form a quantum-critical Dirac fluid in ultraclean graphene, and their electrodynamic responses are described by a universal hydrodynamic theory. The hydrodynamic Dirac fluid can host intriguing collective excitations distinctively different from those in a Fermi liquid[1]. Here, we report the observation of the hydrodynamic plasmon and energy wave in ultraclean graphene. We employ the on-chip terahertz (THz) spectroscopy technique to measure the THz absorption spectra of a graphene micro-ribbon as well as the propagation of the energy wave in graphene close to charge neutrality. We observe a prominent high-frequency hydrodynamic bipolar plasmon resonance and a weaker low-frequency energy wave resonance of the Dirac fluid in ultraclean graphene. The hydrodynamic bipolar plasmon is characterized by the anti-phase oscillation of massless electrons and holes in graphene. The hydrodynamic energy wave is an electron-hole sound mode with both charge carriers oscillating in-phase and moving together. The spatial-temporal imaging technique reveals that the energy wave propagates at a characteristic speed of $V_F/\sqrt{2}$ near the charge neutrality[2-4]. Our observations open new opportunities to explore collective hydrodynamic excitations in graphene systems.

Main text:

Ultraclean graphene provides an attractive platform to explore Dirac fluid physics, where relativistic electrons and holes form a strongly interacting plasma. The electron-electron scattering can dominate over electron-impurity and electron-phonon scatterings in graphene over a substantial temperature range[5], and the many-body system can be well described by a relativistic hydrodynamic theory[1,3,4,6-10]. Electrical transport signatures of the hydrodynamic Dirac fluid in graphene have been observed experimentally, including the hydrodynamic electron flow[11-16], the breakdown of the Wiedemann-Franz law[17], and the quantum-critical conductivity[18]. The hydrodynamic Dirac fluid is also predicted to host intriguing collection excitations, such as hydrodynamic bipolar plasmons and energy waves[1-3,6-9,19-25]. These collective excitations are governed by the strong electron-electron scattering and do not depend on the microscopic details of interactions[2,26]. The hydrodynamic plasmon is a coupled electromagnetic and electron-hole collective excitation with opposite motion of electrons and holes (See Methods). The bipolar nature of this excitation makes it distinct from the conventional monopolar plasmons with only one type of carriers. The hydrodynamic energy wave, also known as the demon mode, is a sound-like mode where the relativistic electrons and holes move in the same direction (See Methods). This energy wave is analogous to the cosmic sound in high energy physics, which gives rise to the large-scale fluctuations observed in the cosmic microwave background radiation, a relic of the "big bang" creating the universe[27]. Such cosmic sound is predicted to propagate at a universal speed of $c/\sqrt{D}$, where D is the dimensionality.

For Dirac electrons in graphene, the energy sound speed should have a value of $V_F/\sqrt{2}$. Although these hydrodynamic collective excitations have been studied extensively in theory[3,4,7,8,22,25], their experimental observation in a solid-state system has so far been challenging.

On-chip THz spectroscopy

Here, we first report the observation of the hydrodynamic plasmon and energy wave in ultraclean graphene micro-ribbons using on-chip time-domain THz spectroscopy. Our technique exploits the subwavelength confinement of THz pulses in a coplanar waveguide, which bridges the large size mismatch between the graphene micro-ribbons with width around 2 μm and the THz photons with wavelength up to 3000 μm.

Figure 1a shows the schematic of our on-chip THz spectroscopy configuration to measure the absorption of a single graphene micro-ribbon (see Methods for details). The THz emitter and detector are integrated onto a single chip together with a co-planar waveguide. We use a double modulation scheme to detect the small changes in the THz transmission due to the micro-ribbon absorption[18]. We modulate the time delay (t) between the THz generation and detection laser pulses at frequency f_1 and detect the resulted modulation in current, which yields low noise measurements of dE/dt. In addition, we modulate the back gate voltage using a square wave (between a finite gate voltage V_G and the charge neutrality voltage V_{CNP} = -0.1 V) at f_2, which allows us to measure the gate-induced THz change $d(\Delta E)/dt$ at the sum frequency $f_1 + f_2$[18].

We first investigate the collective excitations in the graphene micro-ribbon at the base temperature T_0 = 60 K. Figure 1b and 1c show the representative raw data of dE/dt and $d(\Delta E)/dt$ as a function of t at selected gate voltages. The THz absorption spectrum of the micro-ribbon can be calculated as (see Methods for the derivation):

$$A_{V_G}(f) - A_{CNP}(f) \approx -2\,\Re\left(\frac{FFT\left(d(\Delta E)/dt\right)}{FFT\left(dE/dt\right)}\right).$$

Here, FFT represents fast Fourier transform, $A_{V_G}(f)$ is the absorption spectrum at gate voltage V_G, and $A_{CNP}(f)$ is the absorption spectrum at charge neutrality. We measure $A_{V_G}(f) - A_{CNP}(f)$ at different values of V_G. In these data, $A_{CNP}(f)$ is a fixed background which can be obtained by a global fitting of all absorption spectra (see Methods for details). $A_{V_G}(f)$ can then be obtained using the fixed background subtraction.

Figure 1d displays the absorption spectra $A_{V_G}(f)$ as a function of frequency and gate voltage. The data exhibit strong gate-dependent absorption peaks. At electron temperature $T_e = T_0$ the Dirac liquid regime characterized by ¿$\mu \vee$¿T_e is rather narrow (red bar in Fig. 1d). At $|V_G - V_{CNP}| > 0.03$ V, the sample is already in the Fermi liquid regime with $|\mu| > T_e$. The terahertz responses are thus dominated by the plasmon resonance of the Fermi liquid, which shifts to higher energy and gains oscillator strength with increasing carrier density. This behavior is consistent with the Fermi liquid plasmon in graphene observed in previous studies[28,29]. However, we note that the plasmon resonance persists in the Dirac liquid regime near charge neutrality (Figure

2f). This provides the first sign of the collective behavior of the thermally excited electrons and holes.

To understand the absorption data, we perform full-wave electromagnetic simulations using the finite-difference time-domain (FDTD) method (see supplementary information). We use the local conductivity approximation and assume that the graphene conductivity is described by the two-fluid model from ref. 3,

$$\sigma = D_Z \pi^{-1} \left({\tau_{ee}}^{-1} + {\tau_d}^{-1} - i 2\pi f \right)^{-1} + D_F \pi^{-1} \left({\tau_d}^{-1} - i 2\pi f \right)^{-1}.$$

Here D_Z and D_F are the Drude weights of the zero- and finite-momentum modes, and ${\tau_{ee}}^{-1}$ and ${\tau_d}^{-1}$ are the electron-electron and disorder scattering rates[30], respectively. This local conductivity model can capture both the Fermi liquid plasmon and the Dirac fluid hydrodynamic plasmon, but not the energy waves of the Dirac fluid. Figure 2e and 2g show the calculated micro-ribbon absorption spectra. The overall doping dependence in the simulation agrees well with the experimental data, which reaffirms our technique as a reliable approach to characterize the THz response of the graphene micro-ribbon.

Hydrodynamic bipolar plasmon

Next, we probe hydrodynamic plasmons and energy wave excitations of graphene at elevated electron temperatures. This is achieved by transiently heating the micro-ribbon with a femtosecond pump pulse (Fig. 1a)[18], which keeps the lattice near T_0 and helps avoid the unwanted electron-phonon scattering in an equilibrium heating approach. After pumping, the electron system rapidly (~150 fs) thermalizes to a high electron temperature and equilibrates with a bath of optical phonons[31,32]. These

phonons decay over 1 to 2 ps[33,34], returning the lattice to near-equilibrium and lowering T_e to below the optical phonon emission threshold. Following this rapid cooling, a much slower (tens of ps) cooling period ensues[35-37]. We can thus study the temperature-dependent absorption by timing our probe THz pulse to arrive at the sample at different times during the slow-cooling period[35-37]. By synchronizing the optical heating pulse with the gate modulation (see Methods) we can measure $A(f)_{V_G,T_e}-A(f)_{CNP,T_0}$, where $A(f)_{V_G,T_e}$ is the graphene absorption spectrum at different gate voltages V_G and electron temperatures T_e, and $A(f)_{CNP,T_0}$ is the fixed CNP absorption spectrum at the reference temperature T_0. Again, the fixed $A(f)_{CNP,T_0}$ is determined through the global fitting of all THz spectra, after subtracting which we can determine $A(f)_{V_G,T_e}$. Figure 2a-d show the gate-dependent absorption spectra taken at various delays between the optical heating pulse and the THz probe corresponding to different electron temperatures.

The elevated electron temperatures lead to dramatic changes in the plasmon excitation and the associated THz absorption in graphene. The most prominent plasmon features match well with the simulation results based on the local two-fluid model described above (Fig. 2g-j). Based on the comparison with simulations, we can estimate the electron temperature to be 300 K at 10 ps delay, which then decays to 260 K, 210 K,

and 105 K at 20 ps, 30 ps, and 12.5 ns delay, respectively.

Figure 2e shows THz absorption spectra for several different carrier densities at T_e = 300 K. It shows behaviors distinct from those at T_e = 60 K (Fig. 1f). At T_e = 300 K graphene is in the Dirac liquid regime for most of the measured carrier densities (red bar in Fig. 2a). The THz spectra show two features, one strong peak at high frequency and a much weaker shoulder at low frequency. The strong high frequency resonance corresponds to the hydrodynamic plasmon of the Dirac fluid, and it can be captured by the local two-fluid model simulation (Fig. 2g). The weak low frequency resonance can be attributed to the energy wave excitation of the Dirac fluid.

We first examine the high frequency hydrodynamic plasmon of the Dirac liquid at T_e = 300 K (Fig. 2a and e). The plasmon resonance frequency barely changes with the charge density in the hydrodynamic Dirac liquid regime (from V_G = -0.73 V to V_G = 0.53 V), and it starts to increase at higher charge densities (V_G = 0.8 V) when entering the Fermi liquid regime. This hydrodynamic plasmon behavior is distinctly different from the monopolar plasmon of the Fermi liquid at 60 K (Fig. 1f), where the plasmon frequency increases rapidly with doping, especially at the low-density limit.

Figure 2f shows the plasmon resonance frequency as a function of doping at different T_e, where a smooth crossover between the high-temperature Dirac liquid hydrodynamic plasmon (i.e. weak doping dependence) to low-temperature Fermi liquid plasmon behavior (i.e. strong doping dependance) is observed. Interestingly the plasmon frequency at finite electron doping (V_G = 0.8 V) shows a red shift with increasing T_e and thus increasing total carrier density. This anomalous behavior –a

lower plasmon frequency with a larger total carrier density –is a striking signature of the hydrodynamic plasmon at the Dirac liquid to Fermi liquid crossover[1,3,24]. The density and temperature dependence of the hydrodynamic plasmon agrees well with the local two-fluid conductivity model simulation (Fig. 2l).

Demon resonance in graphene micro-ribbon

At low frequency, we also notice a weak dispersive feature in the absorption. Figure 3a-d zoom in the low frequency region of the data in Fig. 2a-d. The color bar is changed to increase the contrast of the low frequency responses. A weak dispersive low-frequency resonance below the hydrodynamic plasmon excitation can be observed in the Dirac liquid regime at T_e = 300 K (Fig. 3a) and T_e = 260 K (Fig. 3b). Such an isolated low-frequency resonance is not observed at T_e = 105 K (Fig. 3d), where the Fermi liquid regime covers most of the measured range and the plasmon resonance appears at a rather low frequency at low carrier concentrations. Similar absorption features are observed in a second device with the same design (see supplementary information).

This low-frequency resonance is a signature of the energy wave, also known as the demon mode, of the Dirac liquid at high electron temperatures. The energy wave arises from hydrodynamic responses of the Dirac liquid with the conservation of energy, momentum, and charge in the electron system[1,3,4,22,26]. At charge neutrality, this mode is a collective in-phase oscillation of the electron-hole plasma and has a characteristic linear dispersion and universal speed of $V_F/\sqrt{2}$ independent of other microscopic details[2]. However, it has zero dipole moment and thus does not couple to

the electromagnetic field. On the other hand, the energy wave can couple to the charge oscillation at finite doping, which results in a blue shift of the resonance frequency and a finite THz absorption. In the high electron density limit (i.e. Fermi liquid regime), this energy wave mode eventually merges with the plasmon resonance[6,8]. The charge-coupled energy wave exhibits strong temperature dependence due to the thermal nature of the resonance.

Demon propagation in graphene

The low-frequency absorption feature in Fig. 3 is rather weak due to the small oscillator strength of the energy wave. To conclusively establish the existence of the energy wave and examine its physical properties, it is desirable to selectively excite the energy wave and directly image its propagation behavior. This can be accomplished using a new spatial-temporal imaging technique based on the on-chip terahertz spectroscopy, as illustrated in Fig. 4a and 4b. Figure 4a shows a cross-section view of the graphene device configuration. A monolayer graphene sheet (15 × 60 μm) was encapsulated between two hBN layers. The hBN (50 nm)/graphene/hBN (80 nm) heterostructure is placed on top of a pair of 50 nm thick gold waveguide traces, which are laterally separated by a 300 nm wide nanogap. The waveguide also serves as the back gate to change the carrier density in the graphene.

Fig. 4b shows a top view of the whole device and an illustration of spatial-temporal imaging technique. A 532 nm femtosecond laser is focused to a narrow line with lateral width around 1 μm to create an ultrafast local thermal excitation of the electron system in graphene. The thermalization of optically-excited electrons happens on a

femtosecond time scale[31,32,38,39] and thus can be considered as almost instantaneous. In the hydrodynamic regime, this transient heat pulse can propagate as energy waves along the graphene channel[3] (white arrow). In contrast to the THz absorption measurement, the approach here selectively launches the energy wave and avoids the strong background response from the hydrodynamic bipolar plasmon. When the energy wave reaches the waveguide nanogap, it can generate a transient electrical signal (i.e. a THz pulse) in the waveguide. Here the nanogap in the waveguide acts as a THz nanoantenna that converts the local charge oscillation associated with the energy wave in weakly doped graphene[3] to a strong THz electrical signal (See Methods). This terahertz signal will propagate along the waveguide and be detected by the GaAs photoconductive detector. By scanning the position of the line excitation and triggering the GaAs detector using a time-delayed pulse, we can measure the THz electrical signal $E(t,x)$ as a function of the pump position (x) and the time delay (t). This spatial-temporal mapping direct probes the propagation behavior of the energy wave.

Figure 4c shows the optical micrograph of the device close to the graphene region. The red dash box indicates the laser scan range, which is 10 μm away from the gap to avoid direct excitation of the waveguide gap by the laser excitation.

Figure 5a-e show the spatial-temporal evolution of the measured THz signal at different dopings. The graphene temperature is at 300 K in these measurements. A propagating energy wave is clearly observed at all dopings. At extremely low charge density (n ~ 0.1×10^{11} cm^{-2}), the demon mode has a velocity close to $V_F/\sqrt{2}$ (red dashed line in Figure 5a), where $V_F=10^6 m/s$[8]. This propagation speed is a signature

of the thermal sound wave in charge neutral Dirac liquid. As the doping increases, the demon velocity increases rapidly due to the coupling with the charge oscillations in graphene. The width of the propagating feature also becomes narrower with increasing doping, suggesting an increasing quality factor.

We can convert the time-domain electrical signal $E(t,x)$ to the frequency domain through Fourier transform,

$$E(t,x)=\int 2\pi[E(f)e^{iq(f)x}e^{-q'(f)x}]e^{-i2\pi ft}df$$

For each frequency f, the propagation wave has a corresponding wavevector $q(f)$ and a decay constant $q'(f)$. The value of $q(f)$ and $q'(f)$ can be extracted by fitting the linear phase shift and exponential amplitude decay of the signal as a function of position x, respectively (See Methods). This procedure of obtaining frequency-domain information from time-domain data is commonly used in finite difference time-domain (FDTD) studies[40]. Figure 5f and g show the extracted dispersion (q) and damping (q') of the energy wave at different carrier densities. Close to charge neutrality, the energy wave has a linear dispersion with a universal speed close to $V_F/\sqrt{2}$. The damping rate of the energy wave is relatively high, and it increases quickly with frequency. As the doping increases, the energy wave propagates with a faster speed and a smaller spatial decay rate.

In summary, we observed both hydrodynamic plasmons and the hydrodynamic energy waves of Dirac fluid using novel on-chip terahertz spectroscopy techniques. Our study opens new opportunities to explore collective hydrodynamic excitations in low dimensional materials.

References

1 Sun, Z., Basov, D. N. & Fogler, M. M. Universal linear and nonlinear electrodynamics of a Dirac fluid. *Proceedings of the National Academy of Sciences* **115**, 3285-3289 (2018).

2 Lucas, A. & Fong, K. C. Hydrodynamics of electrons in graphene. *Journal of Physics: Condensed Matter* **30**, 053001 (2018).

3 Briskot, U. *et al.* Collision-dominated nonlinear hydrodynamics in graphene. *Physical Review B* **92**, 115426 (2015).

4 Phan, T. V., Song, J. C. & Levitov, L. S. Ballistic heat transfer and energy waves in an electron system. *arXiv preprint arXiv:1306.4972* (2013).

5 Geim, A. K. & Novoselov, K. S. in *Nanoscience and technology: a collection of reviews from nature journals* 11-19 (World Scientific, 2010).

6 Levitov, L., Shtyk, A. & Feigelman, M. Electron-electron interactions and plasmon dispersion in graphene. *Physical Review B* **88**, 235403 (2013).

7 Torre, I. *et al.* Acoustic plasmons at the crossover between the collisionless and hydrodynamic regimes in two-dimensional electron liquids. *Physical Review B* **99**, 144307 (2019).

8 Narozhny, B., Gornyi, I. & Titov, M. Hydrodynamic collective modes in graphene. *Physical Review B* **103**, 115402 (2021).

9 Sun, Z., Basov, D. & Fogler, M. Adiabatic amplification of plasmons and demons in 2D systems. *Physical review letters* **117**, 076805 (2016).

10 Moll, P. J., Kushwaha, P., Nandi, N., Schmidt, B. & Mackenzie, A. P. Evidence for hydrodynamic electron flow in PdCoO2. *Science* **351**, 1061-1064 (2016).

11 Ku, M. J. *et al.* Imaging viscous flow of the Dirac fluid in graphene. *Nature* **583**, 537-541 (2020).

12 Bandurin, D. A. *et al.* Fluidity onset in graphene. *Nature communications* **9**, 1-8 (2018).

13 Bandurin, D. *et al.* Negative local resistance caused by viscous electron backflow in graphene. *Science* **351**, 1055-1058 (2016).

14 Berdyugin, A. I. *et al.* Measuring Hall viscosity of graphene's electron fluid. *Science* **364**, 162-165 (2019).

15 Krishna Kumar, R. *et al.* Superballistic flow of viscous electron fluid through graphene constrictions. *Nature Physics* **13**, 1182-1185 (2017).

16 Jenkins, A. *et al.* Imaging the breakdown of ohmic transport in graphene. *arXiv preprint arXiv:2002.05065* (2020).

17 Crossno, J. *et al.* Observation of the Dirac fluid and the breakdown of the Wiedemann-Franz law in graphene. *Science* **351**, 1058-1061 (2016).

18 Gallagher, P. *et al.* Quantum-critical conductivity of the Dirac fluid in graphene. *Science* **364**, 158-162 (2019).

19 Narozhny, B. N. Electronic hydrodynamics in graphene. *Annals of Physics* **411**, 167979 (2019).

20 Lucas, A. & Sarma, S. D. Electronic sound modes and plasmons in hydrodynamic two-dimensional metals. *Physical Review B* **97**, 115449 (2018).
21 Kiselev, E. I. & Schmalian, J. Nonlocal hydrodynamic transport and collective excitations in Dirac fluids. *Physical Review B* **102**, 245434 (2020).
22 Lucas, A. Sound waves and resonances in electron-hole plasma. *Physical Review B* **93**, 245153 (2016).
23 Dufty, J., Luo, K. & Wrighton, J. Generalized hydrodynamics revisited. *Physical Review Research* **2**, 023036 (2020).
24 Svintsov, D. Hydrodynamic-to-ballistic crossover in Dirac materials. *Physical Review B* **97**, 121405 (2018).
25 Fateev, D. & Popov, V. Hydrodynamic Terahertz Plasmons and Electron Sound in Graphene with Spatial Dispersion. *Semiconductors* **54**, 941-945 (2020).
26 Svintsov, D., Vyurkov, V., Yurchenko, S., Otsuji, T. & Ryzhii, V. Hydrodynamic model for electron-hole plasma in graphene. *Journal of Applied Physics* **111**, 083715 (2012).
27 Anderson, L. *et al.* The clustering of galaxies in the SDSS-III Baryon Oscillation Spectroscopic Survey: baryon acoustic oscillations in the Data Releases 10 and 11 Galaxy samples. *Monthly Notices of the Royal Astronomical Society* **441**, 24-62, doi:10.1093/mnras/stu523 (2014).
28 Woessner, A. *et al.* Highly confined low-loss plasmons in graphene–boron nitride heterostructures. **14**, 421-425 (2015).
29 Ni, G. *et al.* Fundamental limits to graphene plasmonics. **557**, 530-533 (2018).
30 Müller, M., Fritz, L. & Sachdev, S. Quantum-critical relativistic magnetotransport in graphene. *Physical Review B* **78**, 115406 (2008).
31 Gierz, I. *et al.* Snapshots of non-equilibrium Dirac carrier distributions in graphene. *Nature materials* **12**, 1119-1124 (2013).
32 George, P. A. *et al.* Ultrafast optical-pump terahertz-probe spectroscopy of the carrier relaxation and recombination dynamics in epitaxial graphene. **8**, 4248-4251 (2008).
33 Yan, H. *et al.* Time-resolved Raman spectroscopy of optical phonons in graphite: Phonon anharmonic coupling and anomalous stiffening. *Physical Review B* **80**, 121403 (2009).
34 Kang, K., Abdula, D., Cahill, D. G. & Shim, M. Lifetimes of optical phonons in graphene and graphite by time-resolved incoherent anti-Stokes Raman scattering. *Physical Review B* **81**, 165405 (2010).
35 Strait, J. H. *et al.* Very slow cooling dynamics of photoexcited carriers in graphene observed by optical-pump terahertz-probe spectroscopy. *Nano letters* **11**, 4902-4906 (2011).
36 Graham, M. W., Shi, S.-F., Ralph, D. C., Park, J. & McEuen, P. L. Photocurrent measurements of supercollision cooling in graphene. *Nature Physics* **9**,

103-108 (2013).

37 Song, J. C. & Levitov, L. S. Energy flows in graphene: hot carrier dynamics and cooling. *Journal of Physics: Condensed Matter* **27**, 164201 (2015).

38 Mics, Z. *et al.* Thermodynamic picture of ultrafast charge transport in graphene. **6**, 1-7 (2015).

39 Tielrooij, K.-J. *et al.* Photoexcitation cascade and multiple hot-carrier generation in graphene. **9**, 248-252 (2013).

40 Schneider, J. B. J. S. o. e. e. & University, c. s. W. S. Understanding the finite-difference time-domain method. **28** (2010).

41 Bao, W. *et al.* Mapping local charge recombination heterogeneity by multidimensional nanospectroscopic imaging. **338**, 1317-1321 (2012).

Main figure legends:

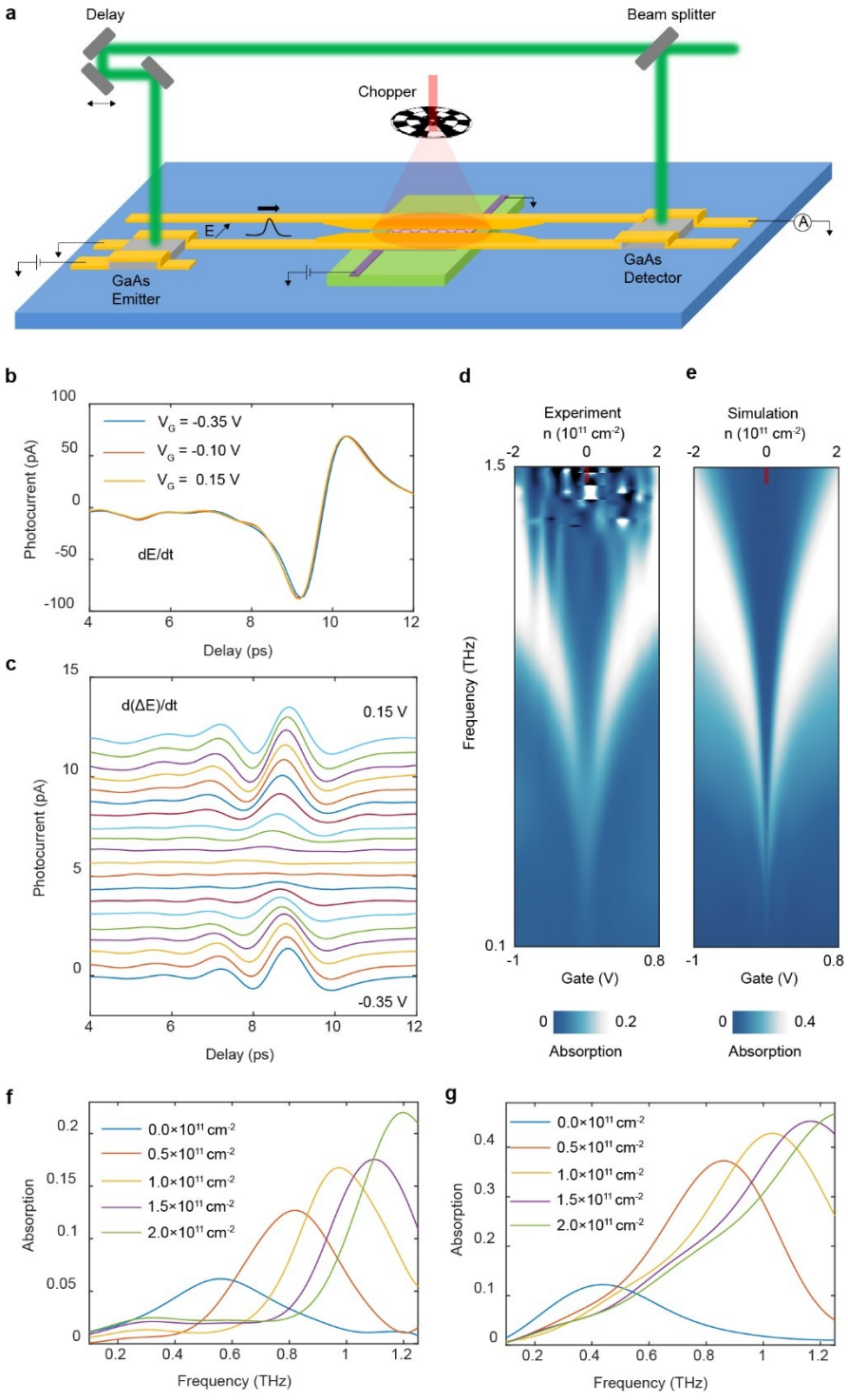

Fig. 1 | Terahertz plasmons in graphene micro-ribbon at 60 K. (**a**) Schematics of the on-chip terahertz spectroscopy experiment to probe the absorption of a single

graphene micro-ribbon. Terahertz emitter and detector are trigged by a 532 nm femtosecond laser. A 1.064 μm femtosecond laser is used to pump the micro-ribbon and transiently increase the electron temperature. The gap in the waveguide is narrowed down near the sample area to increase the coupling efficiency between the waveguide and micro-ribbon. The transmitted pulse is reconstructed by measuring the current collected by the preamplifier as a function of time delay between the laser pulse trains illuminating the emitter and detector. (**b**) Raw data collected at the delay modulation frequency (dE/dt). (**c**) Raw data collected at the sum frequency ($d|\Delta E|/dt$) at gate voltages from -0.35 V to 0.15 V in steps of 0.025 V. Curves are offset for clarity. (**d**) Measured absorption spectra of the graphene micro-ribbon at various gate voltages. (**e**) Micro-ribbon absorption calculated using FDTD simulations. Red bars below the doping axis in (d) and (e) mark the region where ¿$\mu \vee$ ¿T_e. (**f**), (**g**), Line cuts of the absorption spectra at selected carrier densities from experiment and simulation, respectively.

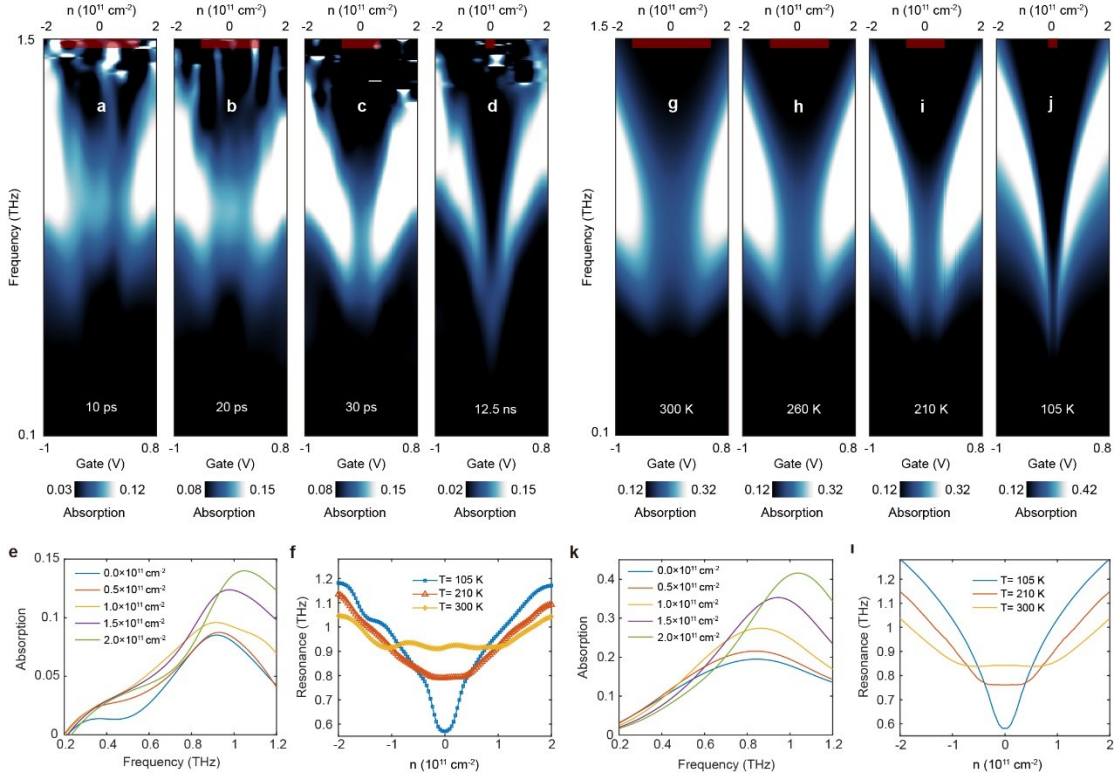

Fig. 2 | Hydrodynamic plasmons in graphene micro-ribbon near charge neutrality. Measured graphene micro-ribbon absorption spectra at (**a**) 10 ps, (**b**) 20 ps, (**c**) 30 ps, and (**d**) 12.5 ns after the pump pulse. The electron temperature decreases from (a) to (d). Red bars below the doping axis mark regions where ¿ $\mu \vee$ ¿ T_e. (**e**) Line cuts of the absorption spectra at selected carrier densities from (a). (**f**) Dispersion of hydrodynamic plasmons extracted from experiment results. (**g-j**) Simulated micro-ribbon absorption spectra at electron temperatures of 300 K, 260 K, 210 K, and 105 K, respectively. Red bars below the doping axis mark regions where ¿ $\mu \vee$ ¿ T_e. (**k**) Line cuts of the absorption spectra at selected carrier densities from (g). (**l**) Dispersion of hydrodynamic plasmons extracted from simulations.

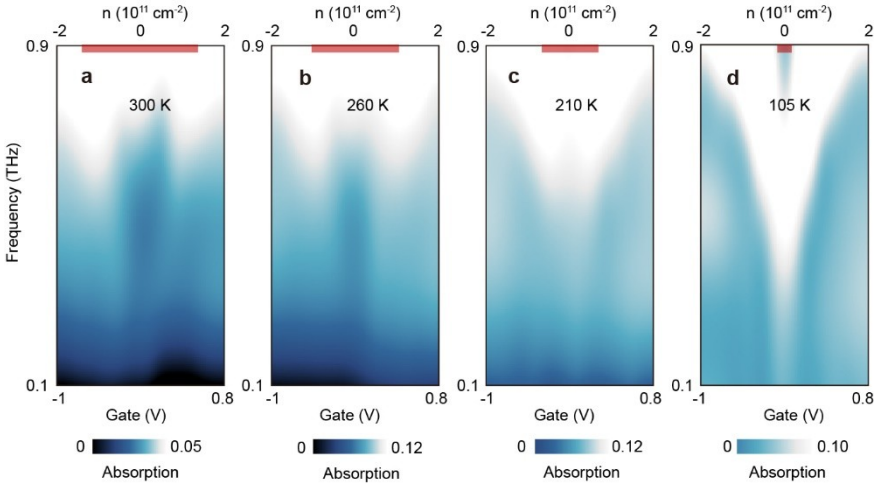

Fig. 3 | Demon mode in graphene micro-ribbon near charge neutrality. Measured graphene micro-ribbon absorption spectra at (**a**) T_e = 300 K, (**b**) T_e = 260 K, (**c**) T_e = 210 K, and (**d**) T_e = 105 K. The images are scaled for better visualization of the low-frequency feature.

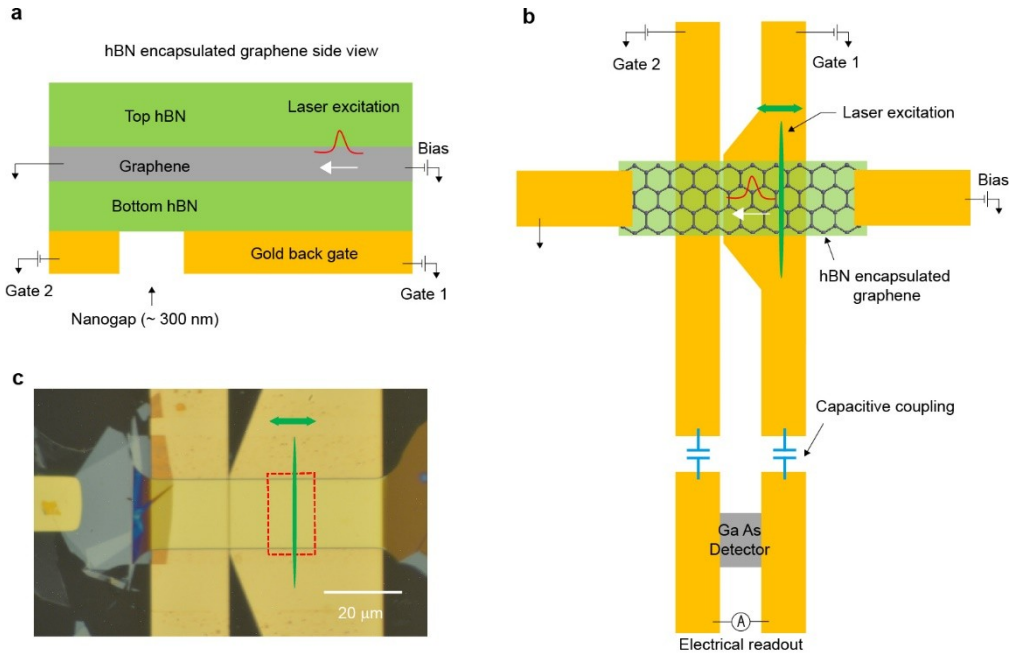

Fig. 4 | Spatial-temporal imaging of demon propagation in graphene. (**a**) Schematic side view of the hBN encapsulated graphene device with gold waveguide serving as back gates. Gate 2 is set to 1.5 V in all the measurements, which corresponds to a carrier density of $n = 4\times10^{11}$ cm^{-2} (See supplementary information). The energy wave is locally launched by a femtosecond laser away from the waveguide gap. It propagates to the nanogap region and induces a THz electrical signal that can be detected by the on-chip THz detector. By scanning the excitation at different positions and measuring the time-delay of the THz signal, the propagation of the energy wave can be determined. (**b**) Schematics top view of the on-chip spatial-temporal imaging technique to image the propagation of demon mode. The waveguide is narrowed down to form a 300 nm wide gap in the region beneath the graphene in order to enhance the electrical field and improve the spatial resolution. The induced THz electrical signal propagates along the waveguide and is detected at the GaAs detector. (**c**) Optical micrograph of the device close to the sample region. The red dashed rectangle indicates the scanning range of the excitation laser, which is more than 10 μm away from the waveguide gap to avoid unintended background from the direct optical excitation in the gap region.

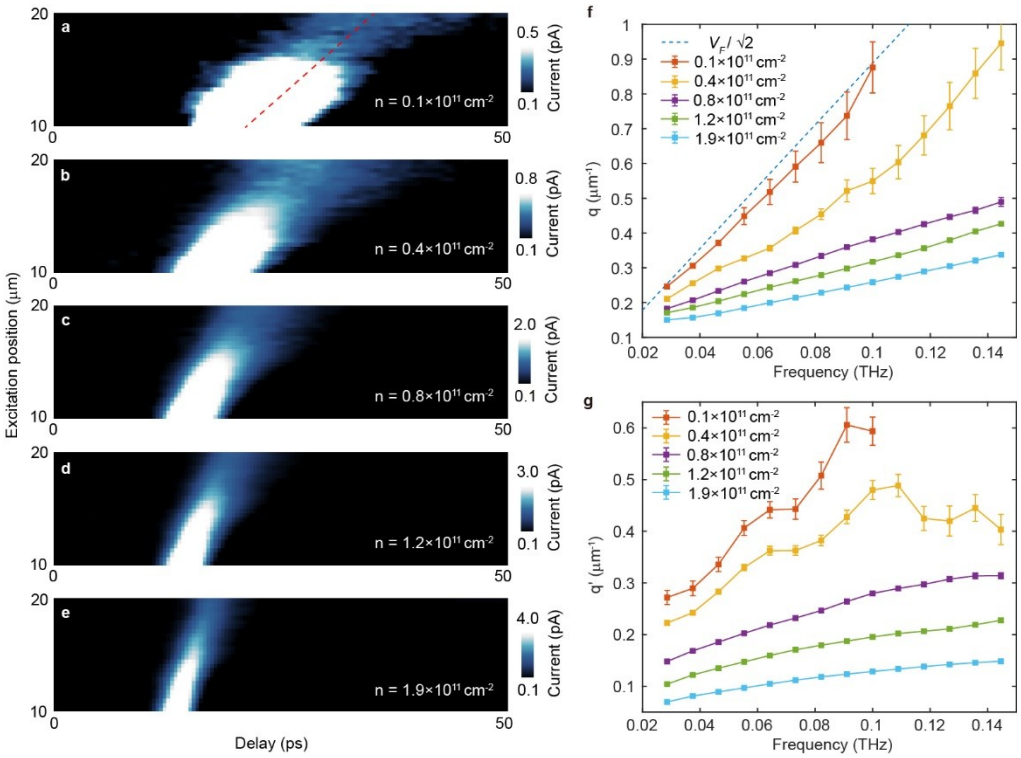

Fig. 5 | Demon propagation in graphene at 300 K. Spatial-temporal imaging data reveal the demon propagation at carrier densities (**a**) n = 0.1×10^{11} cm^{-2}, (**b**) n = 0.4×10^{11} cm^{-2}, (**c**) n = 0.8×10^{11} cm^{-2}, (**d**) n = 1.2×10^{11} cm^{-2}, and (**e**) n = 1.9×10^{11} cm^{-2}. Red dashed line in (a) marks $V_F/\sqrt{2}(V_F=10^6 m/s)$. (**f**) Dispersion and (**g**) damping of the demon mode at various carrier densities extracted from (a)-(e). The blue dashed line marks a linear dispersion with a velocity of $V_F/\sqrt{2}$.

Methods:

Fabrication of graphene samples

We used a dry transfer method with a propylene carbonate (PC) stamp to fabricate the graphene sample. hBN, monolayer graphene, and few layer MoS_2 were first exfoliated onto Si substrates with a 285 nm SiO_2 layer. For the graphene device in Extended Data Fig. 1a, we used the PC stamp to pick up the hBN flake (100 nm), graphene, gate spacer hBN (90 nm), and few layer MoS_2 in sequence. The heterostructure was subsequently released on a fused quartz substrate which has negligible loss in the terahertz frequency range. For the graphene device in Fig. 4c, we used the PC stamp to pick up the hBN flake (50 nm), graphene, gate spacer hBN (80 nm), and then released the heterostructure onto a prepatterned waveguide.

Fabrication of on-chip devices for terahertz spectroscopy measurements

The GaAs flakes were transferred onto the same substrates using PDMS stamps. The positions of the emitter and detector were aligned to make sure the waveguide can overlap with the graphene sample. To suppress unintended reflections of the terahertz pulse from waveguide ends and electrodes, the emitter and detector were placed 1.6 mm apart and far away from both ends of the 7-mm long waveguide. The waveguide traces consist of a 200-nm gold layer on top of a 3-nm Cr layer, patterned using standard photolithography methods and in good contact with the GaAs flakes. Standard e-beam lithography (EBL) was used to make the mask for etching the graphene into narrow micro-ribbons (Extended Data Fig. 1a) or long channel (Fig. 4c). Reactive ion etching (RIE) with CHF_3 and O_2 etching gases (40 sccm and 6 sccm) was used to etch away the hBN. The graphene was then etched with O_2 only. Before fabricating the narrow waveguide on the graphene micro-ribbon, we released another hBN flake (50 nm) on the top surface to avoid direct electric contact between the gold waveguide and graphene.

On-chip THz spectroscopy of graphene micro-ribbon

A 532 nm femtosecond laser (150 fs pulse duration) is split into two beams, which are then focused onto the emitter and detector, respectively (Fig. 1a). Both the emitter and the detector are far away from the waveguide ends, and the distance between them is around 1.6 mm. The large separation between different components avoids the overlap between the main pulse and multiple reflection signals in the time-domain measurements. Only the directly transmitted pulse is collected and analyzed. The substrate is made of fused quartz to minimize unwanted absorption in the THz range. The waveguide consists of two parallel gold traces of 20 μm width separated by a 15 μm gap (Extended Data Fig. 2). The gap is tapered and narrowed down near the sample to enhance the sample-waveguide coupling.

Extended Data Fig. 1a shows the optical micrograph of the device close to the sample region, and Extended Data Fig. 1b shows the sample schematics in the cross-sectional view. An ultraclean graphene micro-ribbon of 2 μm width and 20 μm length is encapsulated in hBN layers. The doping level of graphene is controlled by a back gate made of few-layer MoS_2 for its negligible THz absorption. The waveguide is separated from the graphene by 150-nm-thick hBN.

In each measurement, the biased GaAs emitter is first triggered by a femtosecond laser pulse and becomes highly conductive for ~ 1 ps (as determined by the carrier lifetime of GaAs), creating a quasi-TEM (transverse electromagnetic) THz pulse which travels with minimal dispersion along the waveguide. Then, the detector is activated by a time-delayed laser pulse, allowing a current proportional to the instantaneous local electric field (E) at the detector to be collected by a current preamplifier.

Double modulation method for the absorption measurements

We employ a double modulation method to measure the THz absorption of the graphene micro-ribbon[18]. The time delay between the two laser pulse trains for THz generation and detection is modulated at frequency f_1, while the back gate voltage is

modulated using a square wave at frequency f_2. The detector current is measured at two lock-in frequencies, f_1 and f_1+f_2. These two signals mainly correspond to dE/dt and d(ΔE)/dt, respectively. We then obtain the following quantity after fast Fourier transformation (FFT),

$$\frac{FFT\left(\frac{d(\Delta E)}{dt}\right)}{FFT\left(\frac{dE}{dt}\right)}=\frac{FFT\left(\frac{d(E_{V_G}-E_{CNP})}{dt}\right)}{FFT\left(\frac{d(E_{V_G}+E_{CNP})}{2*dt}\right)}=\frac{2i\omega(\widetilde{E}_{V_G}-\widetilde{E}_{CNP})}{i\omega(\widetilde{E}_{V_G}+\widetilde{E}_{CNP})}. \quad (1)$$

Here $\widetilde{E}_{V_G}$ and $\widetilde{E}_{CNP}$ are the transmitted THz fields as functions of angular frequency ω at finite gate voltage V_G and charge neutrality, respectively. In our experiments, the graphene micro-ribbon only causes a small change to the THz field transmission. In other words, $\widetilde{E}_{V_G}=\widetilde{E}_0(1-\delta_{V_G})$ and $\widetilde{E}_{CNP}=\widetilde{E}_0(1-\delta_{CNP})$, where $\widetilde{E}_0$ is the transmitted THz fields without the graphene micro-ribbon, $\delta_{V_G}\ll 1$, and $\delta_{CNP}\ll 1$. Expanding equation (1) to the leading order in δ, we have

$$\frac{FFT\left(\frac{d(\Delta E)}{dt}\right)}{FFT\left(\frac{dE}{dt}\right)}\approx\delta_{CNP}-\delta_{V_G}. \quad (2)$$

Since the micro-ribbon absorption A= $1-|1-\delta|^2\approx 2\Re(\delta)$, we arrive at the formula used in the main text,

$$A_{V_G}-A_{CNP}\approx 2\Re(\delta_{V_G}-\delta_{CNP})\approx -2\Re\left[\frac{FFT\left(\frac{d(\Delta E)}{dt}\right)}{FFT\left(\frac{dE}{dt}\right)}\right]. \quad (3)$$

For measurements at elevated electron temperature, the pump laser transiently heating the sample is modulated using a chopper in synchronization with the back gate modulation. In this case, we have

$$A_{V_G,T_e}-A_{CNP,T_0}\approx -2\Re\left[\frac{FFT\left(\frac{d(\Delta E)}{dt}\right)}{FFT\left(\frac{dE}{dt}\right)}\right], \quad (4)$$

where A_{V_G,T_e} is the micro-ribbon absorption at back gate voltage V_G and electron

temperature T_e, and A_{CNP,T_0} is the absorption at charge neutrality and base temperature T_0.

Determination of the charge neutrality point

We use a double-modulation of optical pump laser to determine the back gate voltage associated with the charge neutrality point of graphene. At each fixed gate voltage V_G, we modulate the time delay between THz generation and detection at f_1 and the pump laser at f_2. We perform lock-in measurements at f_1 and f_1+f_2, and reconstruct $A_{V_G,T_e}-A_{V_G,T_0}$, the micro-ribbon absorption difference between elevated electron temperature T_e and base temperature T_0 at fixed gate voltage V_G. Since $A_{V_G,T_e}-A_{V_G,T_0}$ is symmetric with respect to the charge neutrality point, the gate voltage of the charge neutrality point can be accurately determined as shown in Extended Data Fig. 3.

Graphene micro-ribbon absorption spectra at charge neutrality

The absorption spectra measured in the experiment is proportional to $A_{V_G}-A_{CNP}$, which contains background from the charge neutrality point. Since this background has a fixed profile for all the gate voltages, we can extract it by fitting the data to a two-Lorentzian model. The spectra can be decomposed into two Lorentzian components, A_{V_G} and A_{CNP} (see Extended Data Fig. 4a). The global A_{CNP} as shown in Extended Data Fig. 4b is obtained by averaging the fitted A_{CNP} over a broad range of gate voltages (0.1-0.8 V). Extended Data Fig. 4c and Extended Data Fig. 4d show the absorption spectra of the graphene micro-ribbon at 60 K before and after the background subtraction, respectively.

Efficient terahertz generation by the energy wave at the nanogap

Our experiment takes advantage of the large field enhancement of the nanogap between the waveguide, similar to near-field spectroscopy experiments[41]. The moving charges associated with the energy wave in weakly doped graphene[3] will induce a negligible terahertz signal in the waveguide when they are above the metal but will

generate a strong terahertz signal when they reach the nanogap.

To demonstrate this effect more quantitatively, we simulate the induced terahertz field in the waveguide generated by a dipole source at different locations. Extended Data Fig. 5a and b show the top and side views of the model used in the FDTD simulations. A dipole source is placed 80 nm (hBN thickness) above the waveguide and a field monitor is used to collect the field in the waveguide 60 μm away from the excitation. We check the collected field as a function of the dipole source position and frequency, as plotted in Extended Data Fig. 5c. Extended Data Fig. 5d shows the linecut of the field amplitude for different excitation positions at 0.1 THz. It is obvious that the terahertz generation becomes strong only when the dipole source is at the nanogap.

Propagation constant of the demon mode in graphene

The frequency domain response of the wave propagation can be extracted through Fourier transform of the time-domain electrical signal $E(t, x)$. Extended Data Fig. 6 and Extended Data Fig. 7 show the extraction of propagation constant $q(f)$ and $q'(f)$ by fitting the linear phase shift and exponential amplitude decay as a function of position *x*, respectively.

Acknowledgements: The on-chip terahertz spectroscopy and theoretical analysis of the work is supported by the Director, Office of Science, Office of Basic Energy Sciences, Materials Sciences and Engineering Division of the US Department of Energy under contract number DE-AC02-05CH11231 (vdW heterostructure Program KCWF16). The device fabrication is supported by the Army Research Office award W911NF2110176. S.C. acknowledges support from Kavli ENSI Heising Simons Junior Fellowship. K.W. and T.T. acknowledge support from the Elemental Strategy Initiative conducted by the MEXT, Japan and the CREST (JPMJCR15F3), JST.

Author contributions: F.W. conceived the research. W.Z. carried out the on-chip

terahertz measurements. S.W. and Z.Z. fabricated the graphene devices. W.Z., S.W., S.C., and F.W. performed data analysis. K.W. and T.T. grew hexagonal boron nitride crystals. F.W., W.Z., S.C., A.Z. wrote the manuscript.

Author information: The authors declare no competing interests. Correspondence and requests for materials should be addressed to fengwang76@berkeley.edu.

Data availability: The data that support the findings of this study are available from the corresponding author upon request.

Extended data figure legends:

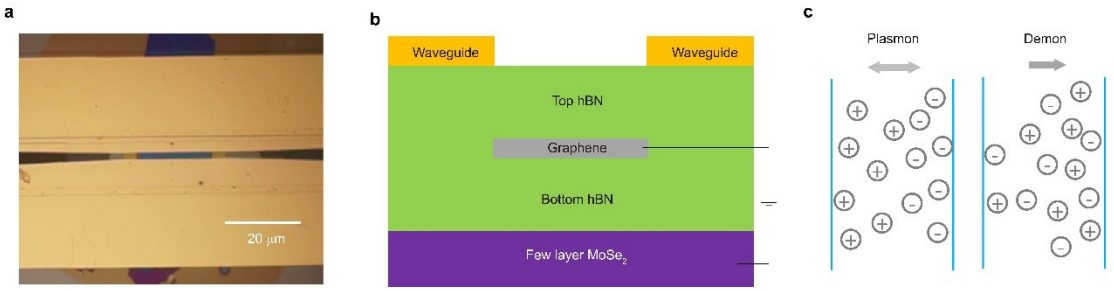

Extended Data Fig. 1 | On-chip terahertz spectroscopy on graphene micro-ribbon. (**a**) Optical micrograph of the device close to the sample region. (**b**) Cross-sectional schematics of the sample under study. The graphene micro-ribbon with 2 μm width and 20 μm length is encapsulated by hBN flakes. The doping level of the micro-ribbon is controlled through a few-layer MoS_2 back gate for its minimal absorption in the terahertz frequency range. (**c**) Illustration of the collective motion of electrons and holes in hydrodynamic bipolar plasmon and demon.

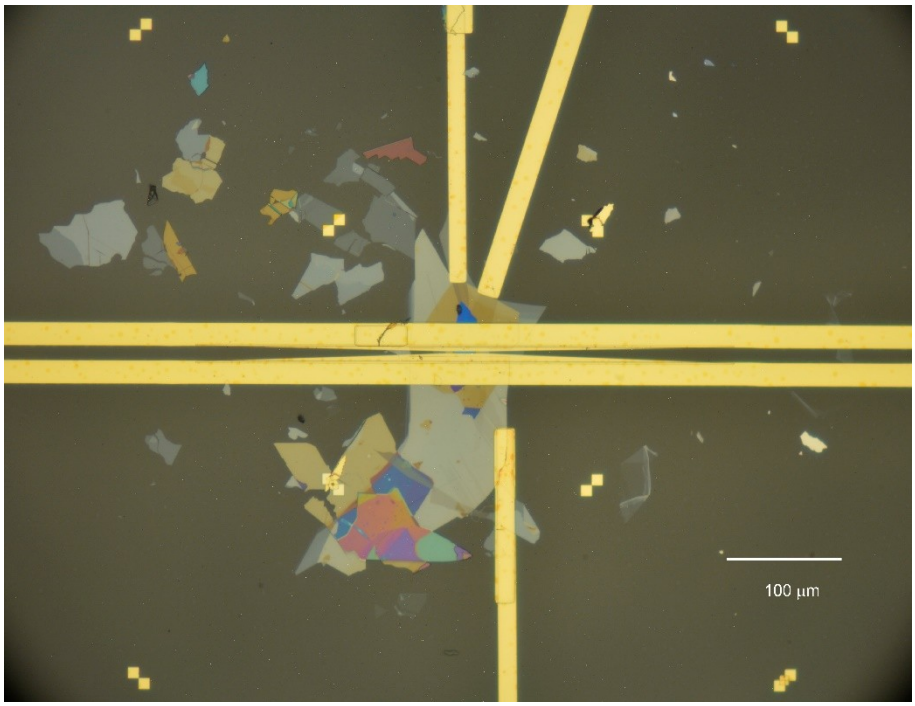

Extended Data Fig. 2 | Optical micrograph of the graphene micro-ribbon device for hydrodynamic plasmon and demon measurements. The waveguide consists of

two parallel gold traces of 20 μm width separated by a 15 μm gap. The gap is tapered and narrowed down near the sample to enhance the sample-waveguide coupling.

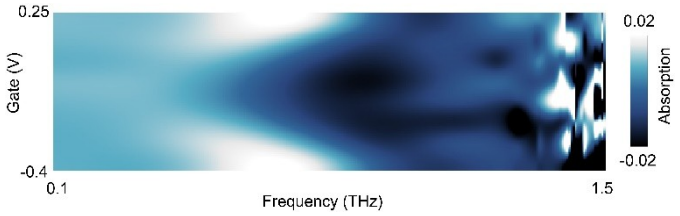

Extended Data Fig. 3 | Temperature difference of the absorption spectra, $A_{V_G,T_e}-A_{V_G,T_0}$, obtained by the double modulation measurement. The absorption shows symmetric profile with respect to V_G= -0.1 V, the back gate voltage associated with the charge neutrality point.

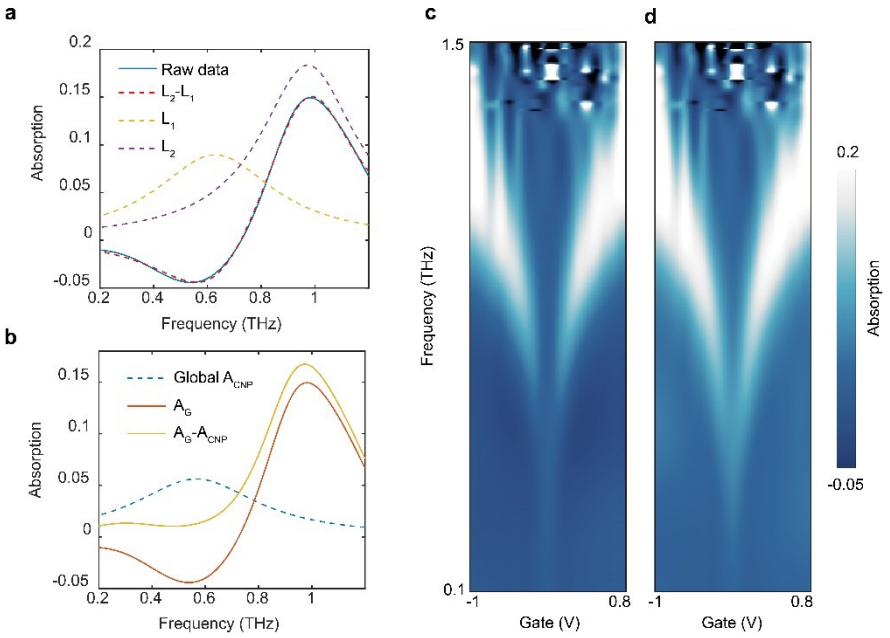

Extended Data Fig. 4 | Determination of A_{CNP} and background subtraction for the absorption spectra. (a) The measured spectrum (solid curve) is fitted to a two-Lorentzian model, where L_1 and L_2 represent the fitted absorption spectra at the charge neutrality point and V_G, respectively. (b) The global background absorption spectra obtained by averaging the fitted A_{CNP} over a broad range of gate voltages from 0.1 V to 0.8 V. (c) Measured $A_{V_G}-A_{CNP}$ at various gate voltages. (d) A_{V_G} obtained by subtracting the global absorption background associated with A_{CNP}.

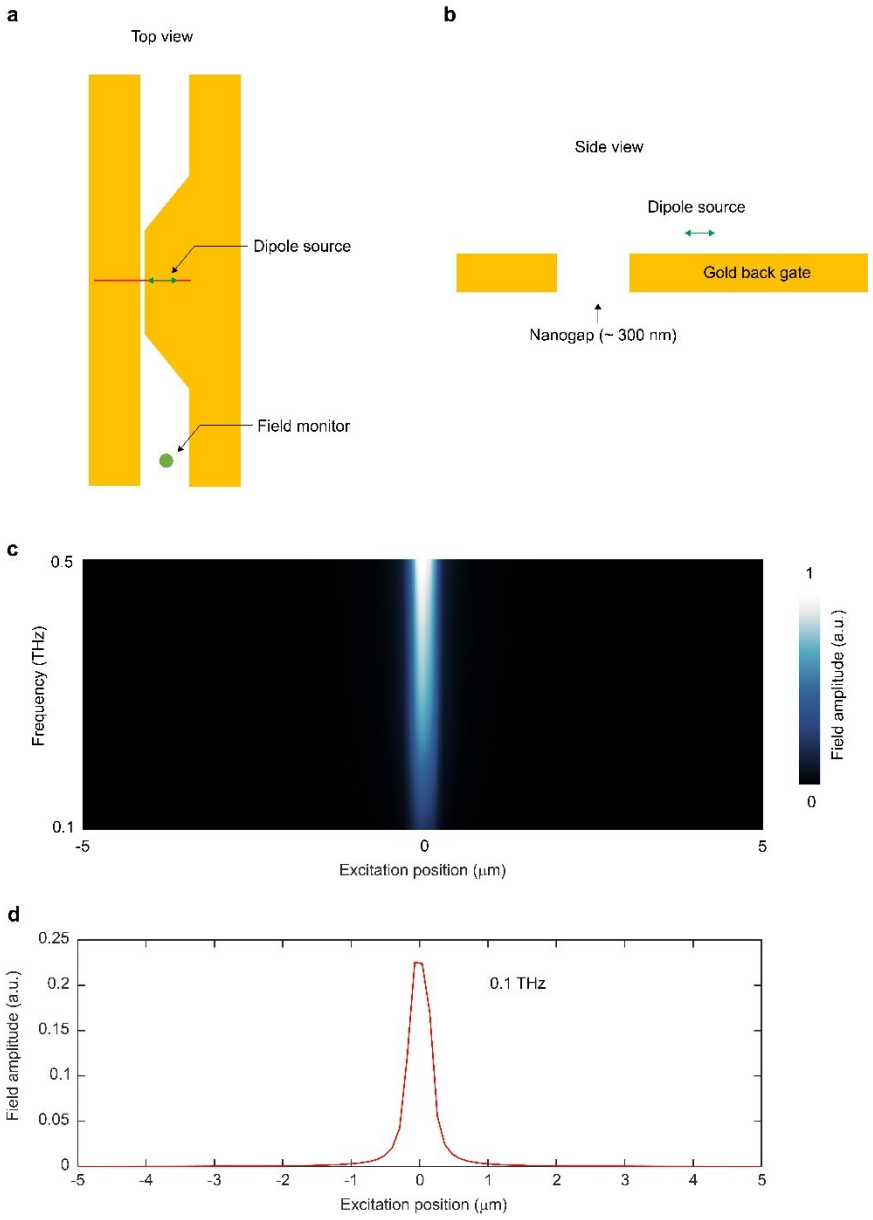

Extended Data Fig. 5 | Field response of the nanogap. Schematic top view (a) and side view (b) of the model used in the FDTD simulations. (c) Field amplitude collected at the monitor position. (d) Linecut of the field amplitude at 0.1 THz.

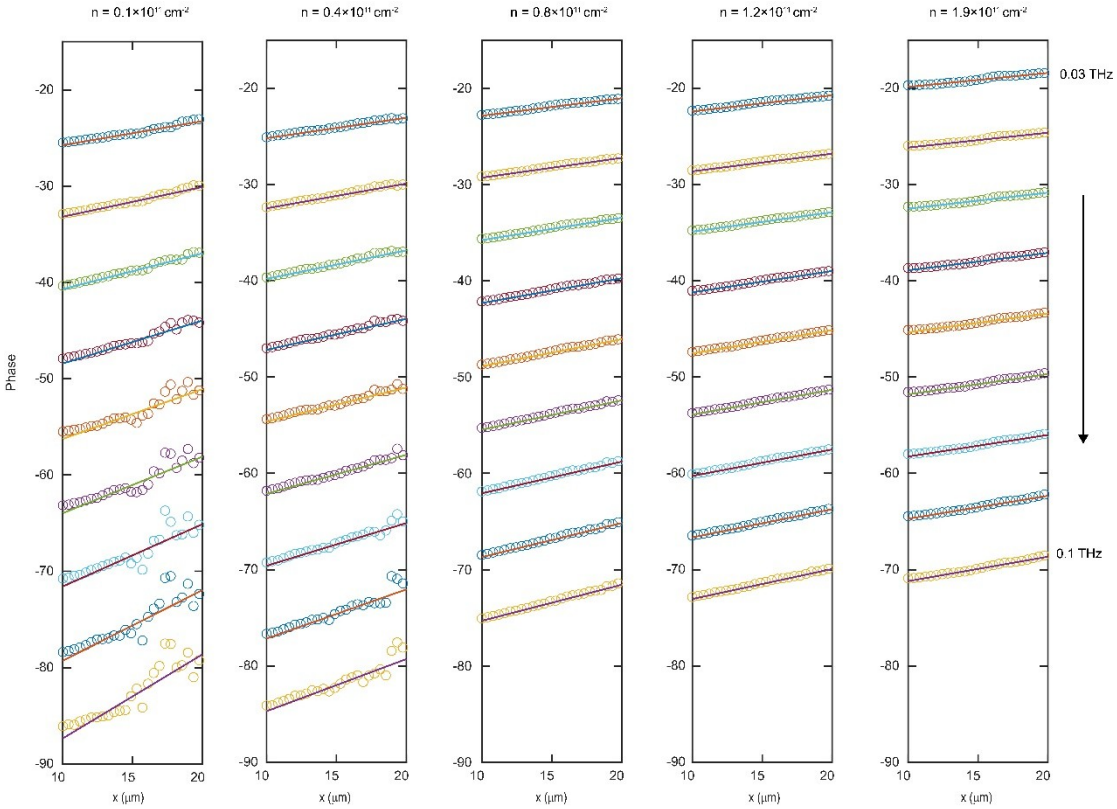

Extended Data Fig. 6 | Linear fit of the phase term along the propagation direction for different carrier densities. From top to bottom the frequency changes from 0.03 THz to 0.1 THz. $q(f)$corresponds to the phase accumulation slope.

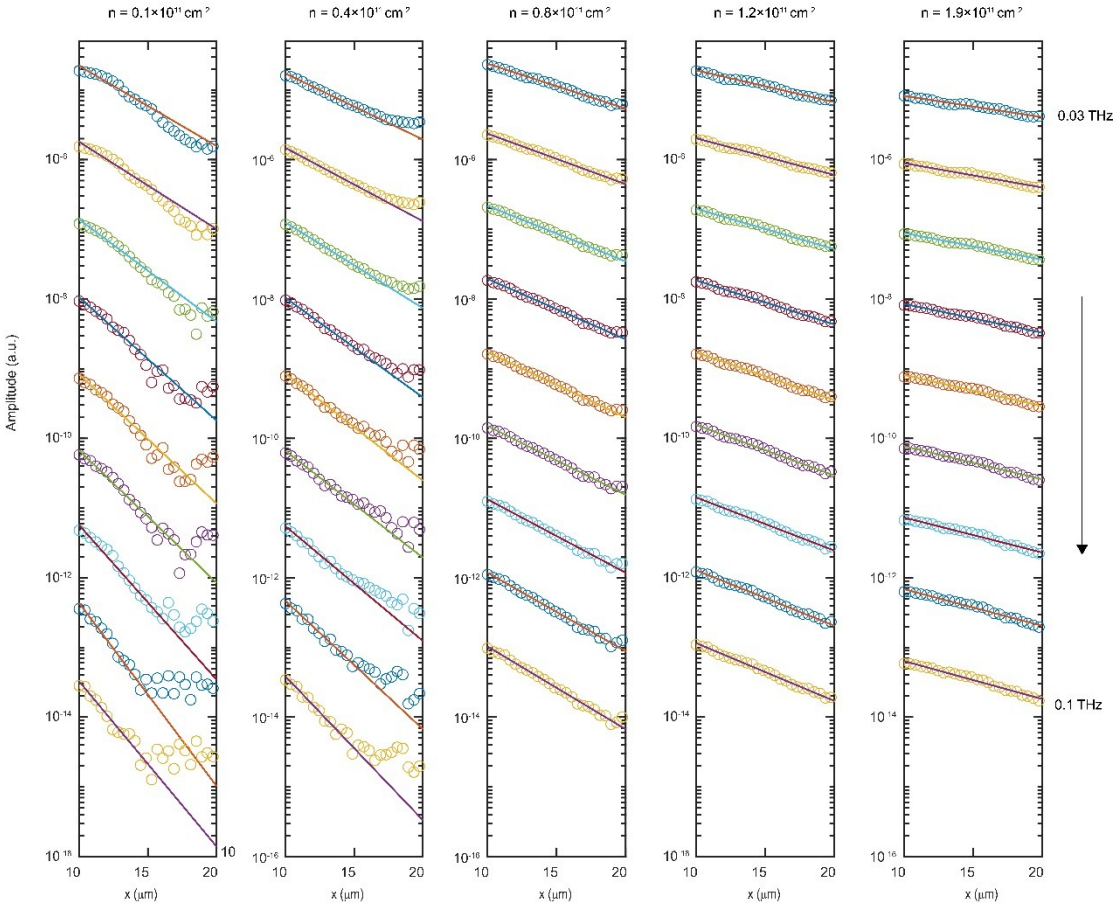

Extended Data Fig. 7 | Exponential fit of the amplitude decay, $q^{'}(f)$, along the propagation direction at different carrier densities. The y axis is plotted in logarithmic scale.